*Article*

**aeroacoustics**

International Journal of Aeroacoustics
2022, Vol. 21(5-7) 521–536

DOI: 10.1177/1475472X221107368
journals.sagepub.com/home/jae
SAGE

# Sound generated by axisymmetric non-plane entropy waves passing through flow contractions

**Dong Yang[1], Juan Guzmán-Iñigo[2] and Aimee S. Morgans[2]**

## Abstract

For a single-component perfect gas, entropy perturbations are associated with the difference between the overall density fluctuation and that coming from the acoustic perturbation. Entropy perturbations can generate sound when accelerated/decelerated by a non-uniform flow and this is highly relevant to thermoacoustic instabilities for gas turbines and rocket engines, and to noise emission for aero-engines. Widely used theories to model this entropy-generated sound rely on quasi-1D assumptions for which questions of validity were raised recently from both numerical and experimental studies. In the present work, we build upon an acoustic analogy theory for this problem. This theory was initiated by Morfey (J. Sound Vib. 1973) and Ffowcs Williams and Howe (J. Fluid Mech. 1975) about 50 years ago and extended recently by Yang, Guzmán-Iñigo and Morgans (J. Fluid Mech. 2020) to study the effect of non-plane entropy waves at the inlet of a flow contraction on its sound generation. Comparisons against both numerical simulations and previous theory are performed to validate the results.

## Keywords

Entropy noise, acoustic analogy theory, thermoacoustic instabilities

Date received: 31 October 2021; accepted: 23 March 2022

## Introduction

In gas turbine and rocket engine combustors, the combustion process is inherently unsteady as both the flow and the chemical reaction process involve turbulence. This unsteady combustion generates heat release fluctuations which are a source of noise,[1] the so-called direct combustion noise. At the

[1]Department of Mechanics and Aerospace Engineering, Southern University of Science and Technology, Shenzhen, China
[2]Department of Mechanical Engineering, Imperial College London, London, UK

**Corresponding author:**
Dong Yang, Department of Mechanics and Aerospace Engineering, Southern University of Science and Technology, 1088 Xueyuan Avenue, Shenzhen 518055, China.
Email: yangd3@sustech.edu.cn

same time, unsteady combustion and the associated unsteady mixing of hot and cold flows also generate advective temperature perturbations (also called "hot/cold spots" or entropy waves). These entropy waves remain silent (decoupled from the acoustics) when they are advected by a uniform flow, but generate sound when they are accelerated.[2–4] This can happen for instance at the turbine inlet in gas turbines or at the downstream nozzle of rocket engines. This entropy generated sound is believed to be a major contributor of indirect combustion noise.[5–7] Indirect noise can modify the thermoacoustic stability of the combustor via its reflected component[8] and increases noise emissions when transmitted outside the engine.

Many theoretical models for entropy noise assume that both the flow and the entropy waves are quasi-one-dimensional. This is the case, for instance, for the theory of Marble and Candel,[2] which predicts the generation of entropy noise using isentropic flow conservation equations across nozzles in the zero-frequency limit. This theory has been extended to higher frequencies by,[9–13] to compositional noise[14,15] and to nozzles with heat transfer.[16]

Recent numerical[17] and experimental[18,19] evidence suggests that approximating entropy perturbations geometrically as plane waves is not satisfactory for real combustors, due to their complex three-dimensional flow, combustion and mixing effects. A recent experimental study further confirms that quasi-1D models may not suffice[20] for these flows.

However, there is little systematic modelling work directed at non-plane wave effects for entropy noise. In,[21,22] it was found that non-plane wave effects were important at medium frequencies and some modelling of their effects was achieved. Other recent efforts to relax the quasi-one-dimensional assumptions have been based on Rapid Distortion Theory,[23] with models developed for the sound generated by entropy interacting with isolated blades[24,25] and cascades.[26]

An alternative way to model the sound generation due to non-plane entropy waves is to use the acoustic analogy theory pioneered by Lighthill.[27,28] Along these lines, the earliest attempts to identify entropy-related sound sources were made nearly 50 years ago by Morfey[29] and Ffowcs Williams and Howe,[30] where the dominant entropy-related sound source term was derived for low Mach numbers. This acoustic analogy theory was recently extended by Yang et al.[31] to give full expressions for the entropy-related sound sources in a single-component calorically perfect gas without external mass, volume force or heat sources and for linear perturbations. It was used[31] to study the entropy noise generated by deceleration through an area expansion, where quasi-one-dimensional, isentropic theory fails.[32]

In this work, we use the acoustic analogy model of Yang et al.[31] to study the sound generated by the acceleration of non-plane incoming entropy waves. The configuration of interest is an area contraction, with a uniform mean flow passing from an upstream cylinder into a smaller co-axial downstream cylinder, being accelerated in this process. Results from the present model are compared to those from Marble and Candel's quasi-1D model and to numerical solutions of the Euler equations.

## Theoretical model

*Governing equations.* We consider a single-component, calorically perfect gas as the working fluid and we assume that the flow is compressible, inviscid and irrotational. Neglecting also any external volumetric sources of mass, momentum and energy, the conservation of mass and momentum can be combined to obtain the following equation[31,33]

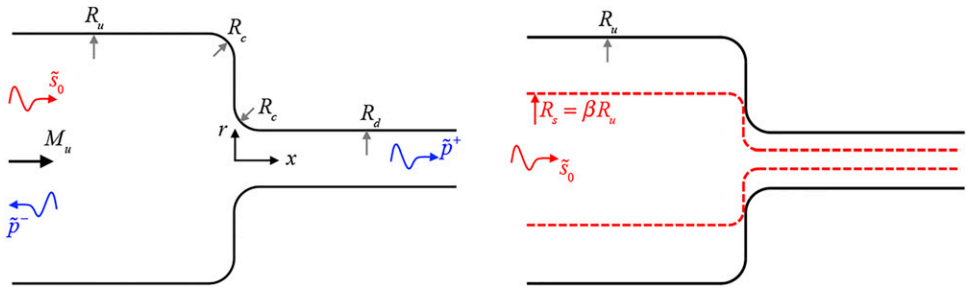


**Figure 1.** (Color online) (Left) The geometric configuration under consideration, which consists of a cylindrical contraction. (Right) Entropy wave at the inlet and its advection envelope through the contraction. $\widetilde{[\,]}$ denotes the Fourier amplitude.

$$\rho \frac{\mathrm{D}}{\mathrm{D}t}\left(\frac{1}{c^2}\frac{\mathrm{D}B}{\mathrm{D}t}\right) - \nabla\cdot(\rho\nabla B) = -\nabla(\rho T\nabla s), \tag{1}$$

where $\rho$, $c$, $T$, $B$, $s$ and $t$ denote density, speed of sound, temperature, stagnation enthalpy, specific entropy and time, respectively. $\mathrm{D}/\mathrm{D}t = \partial/\partial t + \boldsymbol{u}\cdot\nabla$ is the convective derivative and $\boldsymbol{u}$ is the velocity. This equation has considered the energy equation in its entropic form, Ds/Dt = 0.

We now decompose the flow variables into a steady mean, $\overline{[\cdot]}$, and a small-amplitude perturbation, $[\cdot]\prime$, such that $[\cdot] = \overline{[\cdot]} + [\cdot]'$. Following Yang et al.[31] and taking the mean flow to be homentropic, equation (1) can be linearised to obtain

$$\overline{\rho}\frac{\overline{\mathrm{D}}}{\overline{\mathrm{D}}t}\left(\frac{1}{\overline{c}^2}\frac{\overline{\mathrm{D}}B_a'}{\overline{\mathrm{D}}t}\right) - \nabla\cdot\left(\overline{\rho}\nabla B_a'\right) = \nabla\cdot\left(\frac{\nabla\overline{p}}{c_p}s'\right) - \nabla\cdot\left(\overline{\rho}\boldsymbol{u}\frac{\overline{\boldsymbol{u}}\cdot\nabla\overline{T}}{\overline{c}^2}s'\right) - \frac{\overline{\rho\boldsymbol{u}}\cdot\nabla\overline{T}}{\overline{c}^2}\frac{\partial s'}{\partial t}, \tag{2}$$

where $c_p$ denotes the heat capacity at constant pressure, $\overline{\mathrm{D}}/\overline{\mathrm{D}}t = \partial/\partial t + \overline{\boldsymbol{u}}\cdot\nabla$ and $B_a' = p'/\overline{\rho} + (|\boldsymbol{u}|^2/2)'$ denotes the acoustic part of the perturbation in stagnation enthalpy. The left-hand side of equation (2) is an equation governing sound propagation and the three terms on the right-hand side (RHS) are the sound sources due to entropy perturbations.

Neglecting any heat addition, thermal diffusion and viscous effect, the energy equation for a single-component thermally perfect gas gives Ds/Dt = 0. By linearising this equation and further assuming the mean flow to be homentropic, such that $\nabla\overline{s} = \boldsymbol{0}$, the entropy perturbation can be computed after solving the linearised entropy equation

$$\frac{\partial s'}{\partial t} + \overline{\boldsymbol{u}}\cdot\nabla s' = 0. \tag{3}$$

A harmonic ansatz $[\cdot]' = \widetilde{[\cdot]}\,e^{\mathrm{i}\omega t}$ can now be assumed, where $\omega$ is the angular frequency and i the imaginary unit. As discussed in,[31] dimensional analysis of the source terms of equation (2) shows that the second and third terms are $O(M^2)$ and $O(MHe)$ ($He = \omega L/\overline{c}$ where $L$ is some characteristic length scale, such as $R_d$ as shown in Figure 1) times the first term, making them much smaller at low Mach numbers and frequencies. In this work, we focus on low Mach number flows, i.e. $M^2 = 1$, and low frequencies and thus these last two terms can be neglected. At low frequencies, it will also be the case that any mean flow non-uniformity has a much smaller spatial extent than the acoustic wavelength. The effect on the acoustic propagation is small, such that for the LHS terms, $\overline{\rho}$, $\overline{c}$ and $\overline{\boldsymbol{u}}$

can be taken as uniform in each duct ($\overline{\boldsymbol{u}} = \overline{u}\,\mathbf{i}$ where $\mathbf{i}$ is the unit vector in the axial direction). Equation (2) then simplifies to

$$\left[\frac{1}{\overline{c}^2}\left(\mathrm{i}\omega + \overline{u}\frac{\partial}{\partial x}\right)^2 - \nabla^2\right]\tilde{B}_a = \frac{1}{\overline{\rho}}\nabla \cdot \left(\frac{\nabla\overline{p}}{c_p}\tilde{s}\right). \tag{4}$$

The present work applies this theory to a sudden flow contraction between two co-axial connected cylindrical ducts, as shown in Figure 1 (left). The up- and downstream duct radii are $R_u$ and $R_d$, respectively. A uniform mean flow with Mach number $M_u$ enters the larger cylinder inlet on the left-hand side, with the corresponding Mach number in the downstream duct being $M_d$. To avoid velocity singularities in the numerical simulations, the two corners at the junction of the ducts are smoothed with small quarter-circular arcs of radii $R_c$. A small-amplitude entropy wave, $\tilde{s}_0$, is injected at the inlet and then advected downstream as indicated by equation (3). Upon being accelerated through the contraction, reflected ($\tilde{p}^-$) and transmitted ($\tilde{p}^+$) acoustic waves are generated and propagate as plane acoustic waves far upstream and downstream, respectively. The entropy profile imposed at the inlet is axisymmetric, but takes the form of a circular spot rather than a plane wave. It has a uniform value of $\tilde{s}_{\text{inlet}}e^{\mathrm{i}\omega t}$ for radial positions $r \le R_s$ and is zero otherwise. Because the entropy is simply advected by the mean flow, the streamline passing through $r = R_s$ and denoted by the red-dash line in Figure 1 (right) separates two regions: (i) an inner region where entropy is advected and (ii) an outer region with no entropy presence. The position of $R_s$ is given by $\beta = R_s/R_u$. To compare the results obtained with different values of $\beta$, the strength of the entropy profile at the inlet is averaged over the inlet cross-sectional area, such that

$$\left\langle \tilde{s}_0 \right\rangle = \frac{\int_{A_u} \tilde{s}_0 \ \mathrm{d}A}{A_u} = \beta^2 \tilde{s}_{\text{inlet}}. \tag{5}$$

## The solution of the equation

Equation (4) is now solved using the Green's function method[34] for the system shown in Figure 1. The Green's function, $\tilde{G}(\boldsymbol{x}, \boldsymbol{y}; \omega)$, denotes the acoustic response at the location of an observer, $\boldsymbol{x}$, due to a Dirac delta function, $\delta$, at the source location, $\boldsymbol{y}$:

$$\left[\frac{1}{\overline{c}^2}\left(\mathrm{i}\omega + \overline{u}\frac{\partial}{\partial x}\right)^2 - \nabla^2\right]\tilde{G} = \delta(\boldsymbol{x} - \boldsymbol{y}). \tag{6}$$

For a given space $V$, bounded by surfaces $\boldsymbol{s}$ (being positive in the outwards direction), the solution for $\tilde{B}_a$ can be obtained by convolution of the Green's function with the boundary and volume acoustic source terms. Defining $k = \omega/\overline{c}$, this gives

$$\tilde{B}_a = \int_{\partial V}\left(-2\mathrm{i}kM\tilde{G}\tilde{B}_a\mathbf{i} + \tilde{G}\nabla\tilde{B}_a - \tilde{B}_a\nabla\tilde{G}\right) \cdot \mathrm{d}\boldsymbol{s} - \int_V \nabla\tilde{G} \cdot \frac{\nabla\overline{p}}{\overline{\rho}c_p}\tilde{s}\mathrm{d}v. \tag{7}$$

This follows the method of Sec. 2 in[34] where circumferential variations are neglected so that the system is two-dimensional, and the problem is divided into a region upstream of the contraction and a region downstream. Note that in[34] both regions are cylindrical in shape with a sharp transition

between them; in other words, the two rounded edges presented in Figure 1 will be treated as sharp for the acoustic solution. Boundary conditions for the upstream region are that the radial velocity on the cylinder inner surface is zero, the axial velocity oscillation just upstream of the contraction is zero and only outward waves propagate far upstream. Similar boundary conditions are used in the region downstream of the contraction. Then for each cylinder, the Green's function is expressed as a Fourier-Bessel expansion for the cylindrical geometry and the relevant boundary conditions applied, before substituting into (7).

For the acoustic source term, far up- and downstream of the contraction, the entropy disturbance advects within a uniform flow and no acoustic source exists. When the entropy wave passes through the contraction, it accelerates, setting up an acoustic field. This contains many radial modes in the vicinity of the contraction, even though all other than the plane wave mode will be evanescent at low frequencies.

The velocity oscillation at the interface is expanded as the sum of a series of Bessel functions to capture the large number of radial modes – the strength of each "Bessel mode" needs to be solved for. $\tilde{B}_a$ just up- and downstream of the contraction interface are represented in terms of the interface velocity oscillation equation (15) in[34] and the entropic source term, with the latter depending on the mean pressure gradient in both the axial and radial directions. The mean flow profile is assumed to be the same as the geometry profile (no flow separation exists). It was shown in[31] that the mean pressure gradient is predominantly in the axial direction for a flow expansion, and this is also true for the present contraction case. Thus even though the radial gradient can be considered if it is provided (e.g. by numerical simulation), only the axial gradient is retained in the model for simplicity. Additionally, this mean flow is assumed isentropic so that we can use the classical solutions for an isentropic 1D nozzle.

Finally, by applying continuity of $\tilde{B}_a$ across the contraction interface, the velocity oscillation can be resolved. Then $\tilde{B}_a$ and the reflected and transmitted acoustic waves can be obtained.

## Numerical results

In this section, we present the numerical simulations used to validate the model. The numerical method employed here is based on a linearisation of the Euler equations. Both the steady and linearised Euler equations are solved using the finite element method[35] implemented using the open-source computing platform FEniCS.[36,37] The flow variables are assumed axisymmetric. The mean flow is obtained as the solution of the steady, compressible non-linear Euler equations in conservation variables and cylindrical coordinates. The equations are discretised in space using a continuous-Galerkin formulation stabilised using the least-squares method.[35] The discretised non-linear problem is solved using a fully-implicit, pseudo-time-stepping algorithm.[38] A slip boundary condition is imposed on the walls. The mesh used for both the mean flow and the perturbation contains approximately 480, 000 triangular elements. This mesh yields a resolution of around 50 elements per entropy wavelength in the upstream duct for the highest frequency considered in this study, i.e. $He = 0.3$. Quadratic approximation polynomials are employed for both the mean flow and perturbations. The resulting mean flow for the area contraction is depicted in Figure 2 for an inlet Mach number $M_u = 0.069$ ($M_d = 0.204$) and for a ratio of the up- and downstream duct radii of $R_u/R_d = 1.7$. To avoid supersonic velocities at the corners, the radii of the two small quarter-circular arcs were both taken as $R_c = 0.1R_d$.

To obtain the acoustic field, the linearised compressible Euler equations are formulated in primitive variables and recast in the frequency domain, yielding:

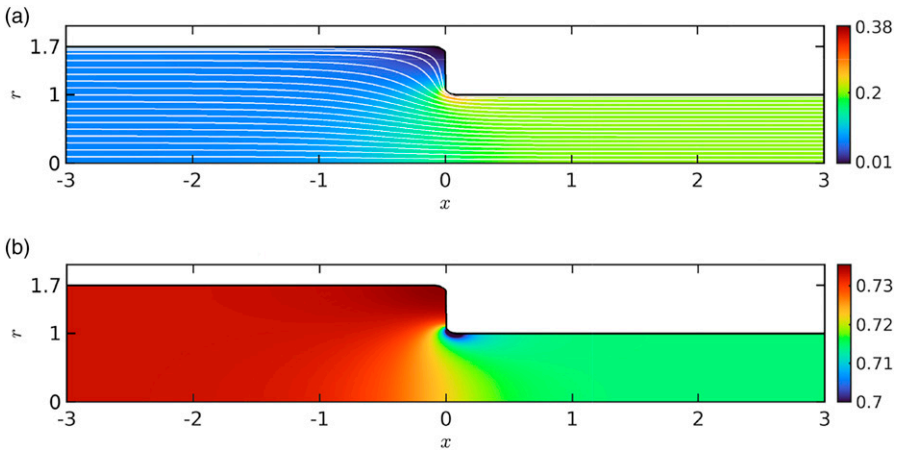


**Figure 2.** (Color online) (a) Mean-flow Mach number, $M$, and (b) normalised mean pressure, $\overline{p}/\gamma\overline{p}_d$,. White lines denote streamlines.

$$\mathrm{i}\omega\tilde{\rho} + \nabla \cdot \left(\overline{\rho}\tilde{\boldsymbol{u}} + \tilde{\rho}\overline{\boldsymbol{u}}\right) = 0, \tag{8a}$$

$$\mathrm{i}\omega\overline{\rho}\tilde{\boldsymbol{u}} + \left(\overline{\rho}\tilde{\boldsymbol{u}} + \tilde{\rho}\overline{\boldsymbol{u}}\right) \cdot \nabla\overline{\boldsymbol{u}} + \nabla \cdot \left(\overline{\rho}\overline{\boldsymbol{u}}\otimes\tilde{\boldsymbol{u}}\right) = -\nabla\tilde{p}, \tag{8b}$$

$$\mathrm{i}\omega\tilde{s} + \overline{\boldsymbol{u}} \cdot \nabla\tilde{s} = 0. \tag{8c}$$

These equations, together with the linearised Gibbs relation $\tilde{p} = \overline{c}^2(\tilde{\rho} + \overline{\rho}\tilde{s}/c_p)$, are spatially discretised using again a continuous-Galerkin formulation stabilised with the least-squares method.[35] The discretisation leads to a linear problem that is solved using the sparse linear solver MUMPS.[39,40] A slip boundary condition is again imposed on the walls. Fully non-reflective acoustic boundary conditions are imposed at both the inlet and the outlet,[41] so that only reflected and transmitted plane acoustic waves exist, respectively, at the far up- and downstream ducts. An entropy perturbation, $\tilde{s}_0$, is inserted at the inlet as a boundary condition. The entropy profile imposed in the simulations is similar to the step function presented in the previous section, but is smoothed to avoid singularities of the gradient at $r = R_s$:

$$\tilde{s}_0(r) = \begin{cases} \tilde{s}_{\text{inlet}} & \text{if} \quad r \le R_s, \\ \tilde{s}_{\text{inlet}}\left[3\left(\dfrac{R_f - r}{R_f - R_s}\right)^2 - 2\left(\dfrac{R_f - r}{R_f - R_s}\right)^3\right] & \text{if} \quad R_s < r \le R_f, \\ 0 & \text{otherwise.} \end{cases} \tag{9}$$

with $R_f = R_s + 0.2$. The distribution of entropy for different frequencies and values of $\beta$ is shown in Figure 3. We observe that for values of $\beta < 1$ and regardless of the frequency, the entropy is zero in the outer region defined by the streamline that passes through $r = R_f$ at the inlet. On the other hand, there is an internal region delimited by the streamline passing through $r = R_s$ at the inlet where the modulus of the entropy is uniform.

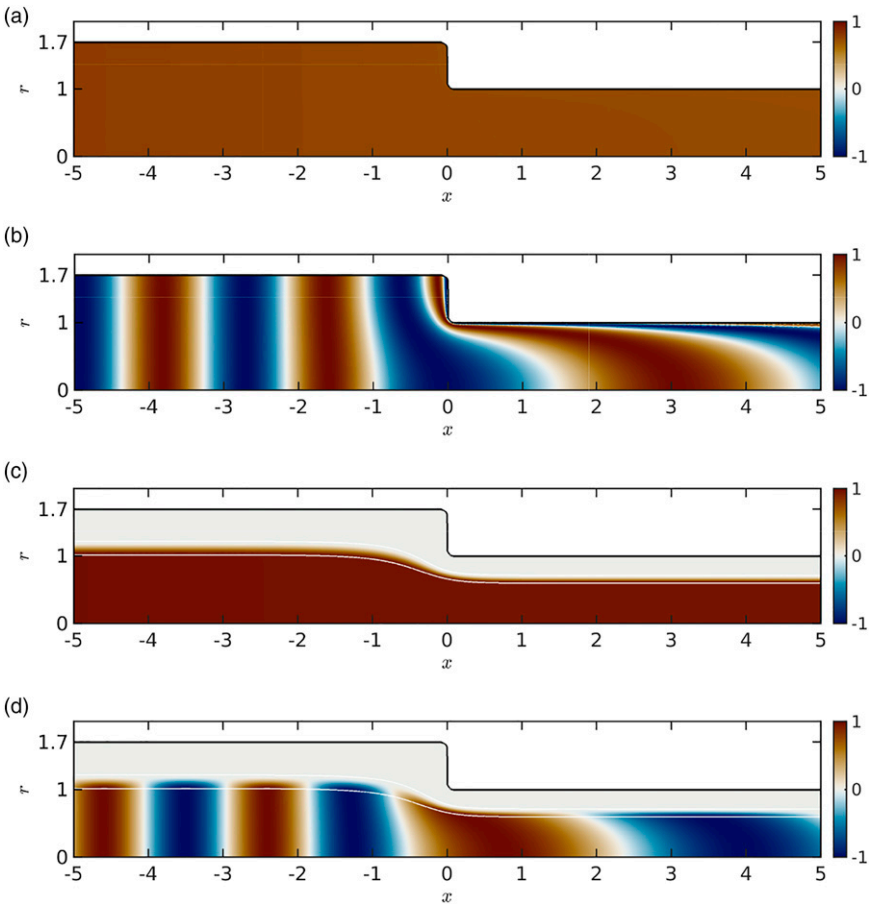


**Figure 3.** (Color online) Real part of the entropy perturbation for: $\beta = 1$ and (a) $He = 10^{-3}$, (b) $He = 0.2$, and $\beta = 0.6$ and (c) $He = 10^{-3}$, (d) $He = 0.2$. The white lines denote the streamlines passing through $r = R_s$ and $r = R_f$ at the inlet.

The acoustic field generated by the acceleration of entropy fluctuations is post-processed using the multi-microphone method[42,43] to compute the reflected and transmitted waves. Figure 4 shows the reflected and transmitted coefficients obtained from the simulations for several values of $\beta$. For all the configurations, both coefficients tend to a constant value at low frequencies (the compact limit) and, when the frequency increases, the values of the coefficients drop due to non-compact effects. This low-pass filter behaviour is typical of entropy noise. The predictions of the compact, 1D and isentropic model of Marble and Candel[2] are also depicted in Figure 4. For a subsonic nozzle, the reflected and transmitted coefficients predicted by this model are respectively

$$\frac{\tilde{p}^{-}/(\gamma\overline{p}_u)}{\langle\tilde{s}_0\rangle/c_p} = -\left(\frac{M_d - M_u}{1 - M_u}\right)\frac{0.5M_u}{1 + 0.5(\gamma - 1)M_uM_d}, \tag{10}$$

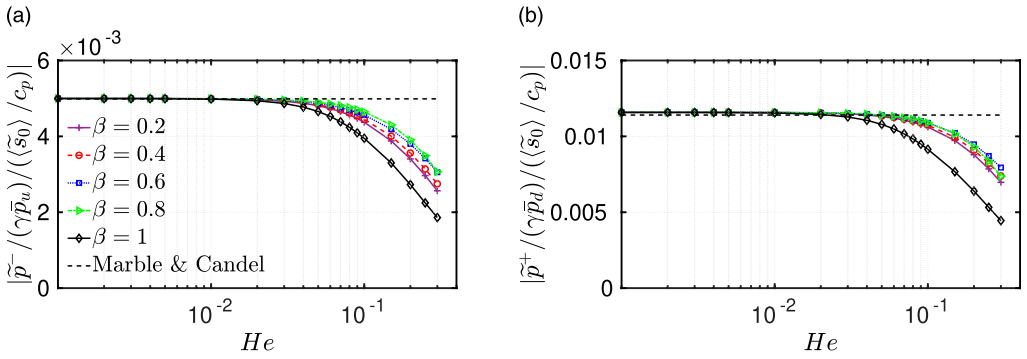


**Figure 4.** (Color online) Acoustic (a) reflection and (b) transmission coefficients produced by the acceleration of entropy waves at the flow contraction depicted in Figure 2. Numerical results (lines with symbols) and predictions of the compact Marble and Candel model[2] (black dashed line).

$$\frac{\tilde{p}^{+}/(\gamma\overline{p}_d)}{\langle\tilde{s}_0\rangle/c_p} = \left(\frac{M_d - M_u}{1 + M_d}\right)\frac{0.5M_d}{1 + 0.5(\gamma - 1)M_uM_d}, \tag{11}$$

where $\gamma = 1.4$ is the adiabatic index. The value of the reflected and transmitted coefficients in the compact limit is the same for all $\beta$, the same for plane entropy waves (defined by $\beta = 1$) and the same as predicted by the Marble and Candel model. Because the simulations and the predictions of the Marble and Candel model tend to the same values at low frequencies, this model will be used in the following section to benchmark the results obtained with the acoustic-analogy-based model.

## Model results

In this section, the acoustic response of the contraction to incoming entropy waves is investigated analytically using the acoustic analogy presented previously. As a reminder, the Green's functions used to solve the acoustics assume sharp edges at the flow contraction and the mean flow profile is assumed to be the same as the geometry profile. For the entropic source term on the RHS of equation (4), the spatial variation of the entropy perturbations, $\tilde{s}$, is required as an input. As observed in Figure 3(a) and (c), phase variations during the advection of entropy through the contraction are negligible at low frequencies. $\tilde{s}$ can thus be considered uniform within the region delimited by the streamline passing through $r = R_s$ at the inlet. In this work, we intend to provide an analytical solution to the problem and hence assume that the streamline path, denoted by the red-dash line in Figure 1 (right), is not explicitly available. Three models are proposed to estimate this path, denoted entropy profile hereafter, as shown in Figure 5. The first, denoted 'Streamline 1D model', assumes a quasi-1D flow within the duct so that the ratio between the entropy profile radius and that of the duct at any axial location is fixed and equal to $\beta$

$$\frac{\widehat{r}_s\left(\widehat{x}\right)}{\widehat{r}_g\left(\widehat{x}\right)} = \frac{R_s}{R_u} = \beta, \tag{12}$$

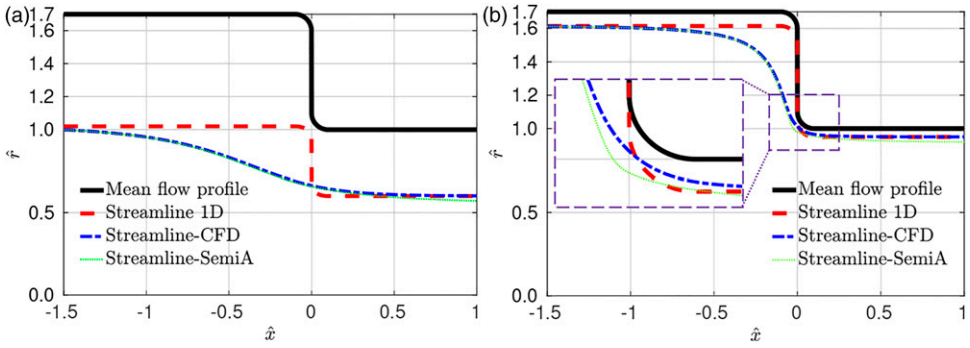


**Figure 5.** (Color online) The flow and entropy profiles, with $\beta$ = 0.6 (left) and $\beta$ = 0.95 (right). $\hat{r} = r/R_d$ and $\hat{x} = x/R_d$.

where $\hat{r}_s(\hat{x})$ and $\hat{r}_g(\hat{x})$ are the normalised radii of the entropy profile and geometry profile at the normalised axial location $\hat{x}$ respectively (with all normalizations being with respect to the radius $R_d$). The second model, denoted 'Streamline-CFD model', uses the axisymmetric streamlines obtained from the numerical mean flow, as depicted in Figure 2. The third model, denoted 'Streamline-SemiA model' uses streamlines for an incompressible potential flow without smoothing circular arcs ($R_c$ = 0). This potential flow field can be obtained by numerically solving Laplace's equation or by solving semi-analytically (by using the Green's function method) the homogeneous version of equation (4) with $\overline{u} = 0$ and assuming the frequency to be very low.[44] ($He = \omega R_d/\overline{c} = 10^{-6}$).

The entropy profiles for $\beta$ = 0.6 and 0.95 as obtained using the three models are shown in Figure 5. Two important points are firstly that the Streamline 1D model gives a very different entropy profile to those from the other two models for both $\beta$ = 0.6 and 0.95. Secondly, the difference between the streamlines from the CFD and the semi-analytical model is small in the case $\beta$ = 0.6 but becomes significant near the inlet edge of the downstream duct when $\beta$ = 0.95.

In order to compare the prediction from the present model with that from Marble and Candel,[2] we introduce the relative difference (for both reflection and transmission coefficients) defined as

$$\text{Difference} = \left| \frac{\text{Present model} \; - \; \text{Marble and Candel model}}{\text{Marble and Candel model}} \right|. \tag{13}$$

We now consider a plane entropy wave, i.e. $\beta = 1$, at the inlet and the Streamline 1D model for the entropy profile. Figure 6 shows that when $R_c/R_d = 0.1$, the difference compared to the Marble and Candel model is about 4%. This increases with $R_c$ and is negligible for $R_c/R_d < 0.02$. This is consistent with the Green's functions assuming cylindrical ducts for which $R_c/R_d$ is zero.

We now take $R_c/R_d = 0.1$, the same value as the simulations, and consider non-planar entropy waves, i.e. $\beta < 1$. Figure 7 shows that for the Streamline 1D model entropy profile, the predictions from the present model deviate significantly from those of the Marble and Candel model when $\beta < 1$, reaching 35% when $\beta \approx 0.7$. However, this difference is greatly reduced if the Streamline-CFD entropy profile is used, for which the largest difference is about 10% at $\beta = 0.95$. In Figure 8, we show that as the corner radius is reduced, the Streamline 1D model entropy profile gives results which better match those from the Streamline-CFD entropy profile (which is always based on $R_c/R_d = 0.1$).

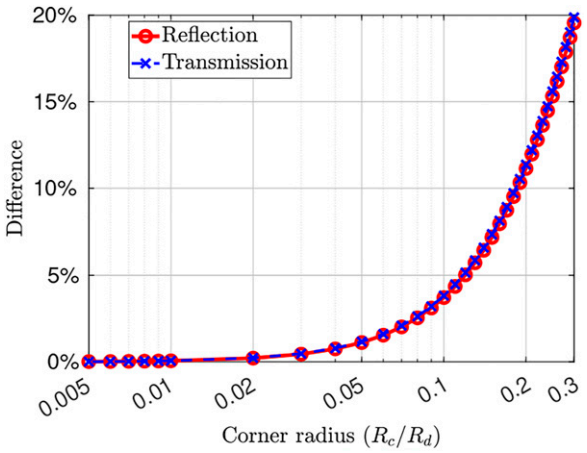


**Figure 6.** (Color online) The effect of the radii of the two corners on the normalised difference between the entropy noise predicted by the present model and Marble & Candel. $\beta = 1$, $M_u = 10^{-3}$ and $He = 10^{-6}$ are considered.

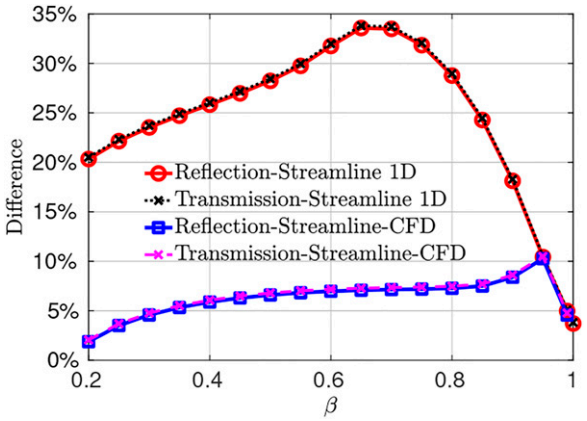


**Figure 7.** (Color online) The effect of $\beta$ on the normalised difference between the entropy noise predicted by the present model and Marble & Candel. $R_c/R_d = 0.1$, $M_u = 10^{-3}$ and $He = 10^{-6}$ are considered.

From Figure 8, it can be seen that by using the Streamline-SemiA entropy profile, a good match to the Marble and Candel model is obtained over the whole range of $\beta$. It is worth noting that at $\beta = 0.95$, the significantly different predictions between the Streamline-CFD model with $R_c/R_d \leq 0.01$ and the Streamline-SemiA model is solely due to the slight difference between the streamlines from the CFD and the semi-analytical model, as shown in Figure 5 (right). This leads to the main conclusion of the paper: for the present flow contraction, the sound generated by non-planar, axisymmetric entropy waves passing through a contraction with sharp corners can be accurately predicted by the Marble and Candel model as long as the entropy wave profile matches the corresponding potential flow streamline. This conclusion is true for low-Mach numbers and low-frequencies.

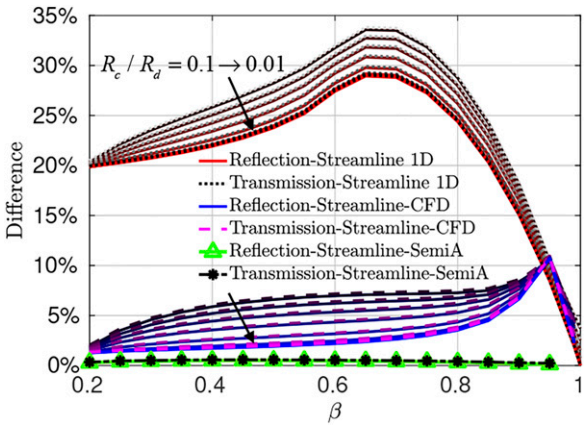


**Figure 8.** (Color online) The effect of $\beta$ when the corner radius $R_c/R_d$ varies. 8 lines with $R_c/R_d$ = 0.1, 0.08, 0.06, 0.04, 0.02, 0.01, 0.007, 0.005 are plotted for each result in the Streamline 1D and Streamline-CFD models while the last three nearly merge into one. $M_u = 10^{-3}$ and $He = 10^{-5}$ are considered.

Next, we compare predictions at the compact limit ($He = 10^{-3}$), from the models with those from the numerical simulations. As shown in Figure 9, in the considered range, $\beta \in [0.2, 1]$, while the present Streamline 1D model predicts higher acoustic reflection and transmission coefficients, both the present Streamline-SemiA model and the Marble and Candel model predict the same results compared with the numerical simulations.

Finally, we consider the effect of frequency dependence. As shown in Figure 3, as $H_e$ increases, the central part of the entropy perturbation is advected through the junction faster than its outer part, and the distribution becomes non-uniform. The low-pass filter behaviour of the acoustic reflection and transmission coefficients was shown in Figure 4. To account for this frequency dependence in the present model, we keep $R_c/R_d = 0.01$ for the mean flow profile and still assume the mean pressure gradient to be nonzero only in the axial direction. We then use the semi-analytically obtained streamline for the entropy profile, but consider the entropy advection within this profile to be two dimensional. This 2D entropy perturbation distribution can be obtained by numerical simulations,[31] or as suggested by,[21] by discretising the radial direction into streamtubes, assuming isentropic 1D flow in each one and integrating the entropy in each to obtain the whole distribution. We use the latter method in the present paper. The results in Figure 10 show that for $H_e < 0.1$, both the LEE and the present model predict similar results to those of the Marble and Candel model. However, for $H_e > 0.1$, both the reflection and transmission coefficients exhibit a gain fall-off. This is captured by both the LEE and the present model, with the discrepancy between the two likely to be associated with the assumption on the mean flow profile and the mean pressure gradient. More accurate predictions would require fully accounting for the 2D nature of the mean pressure gradient and the entropy perturbation distribution, and is left for future study.

It is worth noting that a flow expansion case was considered in.[31] The expansion accounts for the flow separation, whereas the present contraction case assumes attached flow. As can be seen from Figure 10 in the present paper, the non-planar effect becomes apparent when the frequency is higher than $H_e \approx 0.1$, corresponding to a Strouhal number based on the radius of the smaller duct $S_t = \omega R_d/\overline{u}_d \approx 0.5$. For the expansion case, as shown in Figure 3 in,[31] the non-planar effect starts to become apparent at about $S_t \approx 0.04$. The latter frequency (in terms of Strouhal number) is much smaller than the former. The reason for this is because in the expansion case, the flow separates to

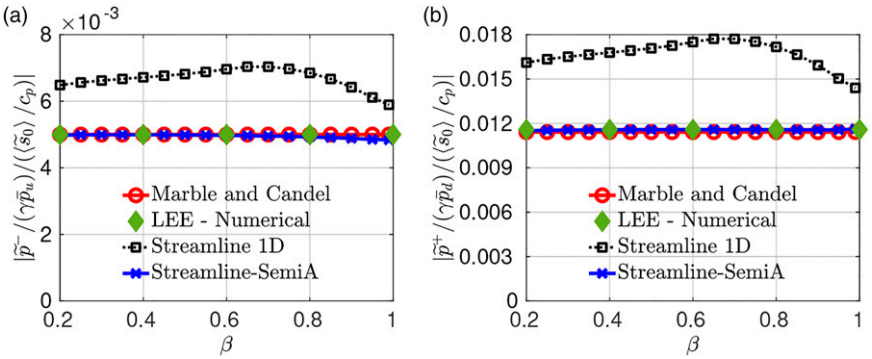


**Figure 9.** (Color online) Acoustic (a) reflection and (b) transmission coefficients due to non-plane entropy waves passing through a flow contraction for $M_u$ = 0.069 ($M_d$ = 0.204). In both the Streamline-CFD and Streamline 1D models, $R_c/R_d$ = 0.1 is used, while for the Streamline-SemiA model, $R_c/R_d$ = 0.01 for the mean flow profile. $He$ = $10^{-3}$.

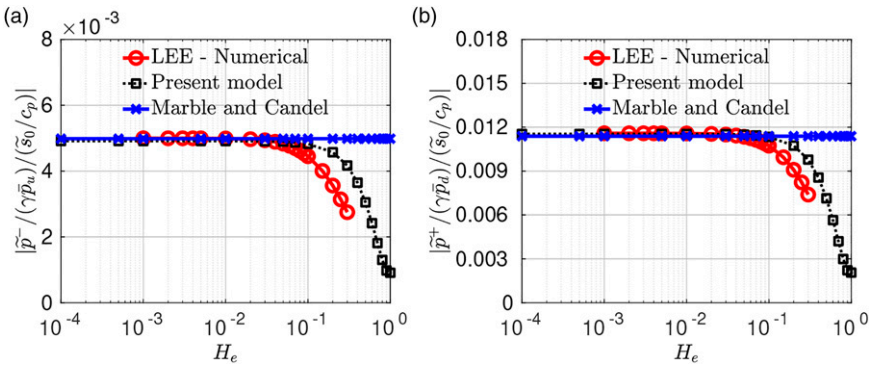


**Figure 10.** (Color online) Acoustic (a) reflection and (b) transmission coefficients due to non-plane entropy waves passing through a flow contraction for $M_u$ = 0.069 ($M_d$ = 0.204). $\beta$ = 0.8 is considered. In the present model, the Streamline-SemiA model with $R_c/R_d$ = 0.01 for the mean flow profile is used.

generate a long recirculation bubble downstream of the area change. This results in a spatial length responsible for the deceleration of the entropy much longer than the spatial length corresponding to the acceleration of the entropy in the contraction case – about 10 times that of the radius of the smaller duct, as can be seen in Figure 2 of,[31] in the expansion case, and about a similar length of the radius of the smaller duct, as shown in Figure 3, in the contraction case. Except for the difference in the non-planar wave effect, the two cases are also different at the low-frequency (compact) limit. The contraction flow result tends to the prediction from Marble and Candel's compact model, while for the expansion flow, the generated noise is much smaller than that from the Marble and Candel model, due to the flow separation and resulting spatial extent of the recirculation zone, as seen in Figure 3 of.[31]

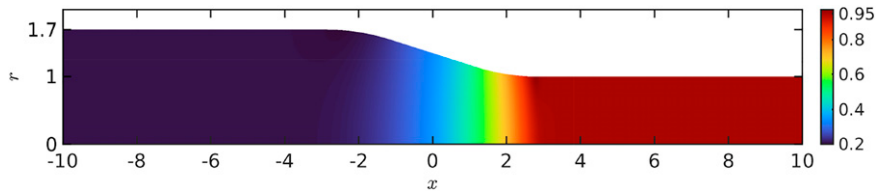


**Figure 11.** (Color online) (a) Mean-flow Mach number, $M$. The Mach number at the inlet is $M_u = 0.205$ and $M_d = 0.95$ at the outlet. $R_u/R_d = 1.7$.

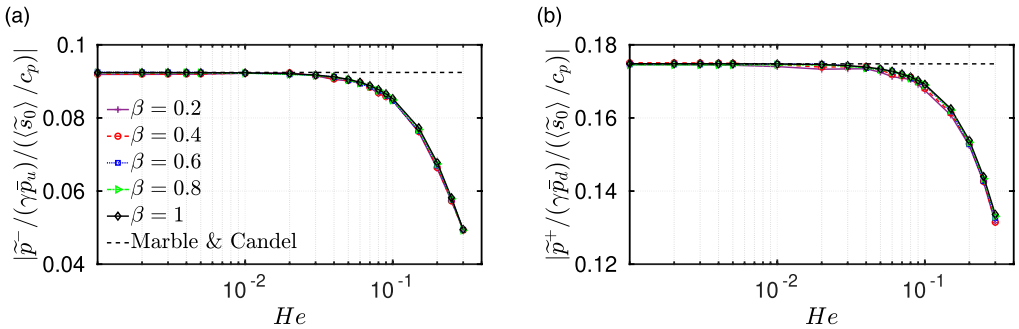


**Figure 12.** (Color online) Acoustic (a) reflection and (b) transmission coefficients produced by the acceleration of entropy waves at the flow contraction depicted in Figure 11. Numerical results (lines with symbols) and predictions of the compact Marble and Candel model[2] (black dashed line).

## *Flow contraction sustaining a high subsonic Mach number flow*

In the previous section, we showed that, in the compact limit, the magnitude of the acoustic waves generated by acceleration of entropy fluctuations through a low-Mach-number flow contraction tend to the Marble and Candel 1D prediction, even if the entropy waves are non-planar. The results presented so far have been obtained for low-Mach-number flows, so that the simplified version of the acoustic analogy could be employed. In this section, we explore numerically a flow contraction sustaining a high subsonic Mach number flow to verify if this observation is also true in this case. We consider an axisymmetric flow contraction characterised by the same ratio of the up- and downstream duct radii as previously, i.e. $R_u/R_d = 1.7$. The geometry is further smoothed to avoid supersonic regions in the corners: the radius of the corners is now taken to be $R_c/R_u = 10$ and a slope of 10 deg with respect to the horizontal axis is introduced at the contraction. A Mach number $M_u = 0.204$ is imposed at the inlet, leading to a Mach number in the downstream duct of $M_d = 0.95$. The geometry and the Mach number distribution are depicted in Figure 11.

The acoustic reflection and transmission coefficients due to entropy acceleration have been computed as described in previous sections and the results are plotted in Figure 12. It is clear that even in the high subsonic Mach number limit, the results at low frequencies are independent of the distribution of entropy at the inlet and that the results tend to the predictions of the Marble and Candel model.

## Conclusion

In the present paper, we have studied both theoretically and numerically the sound generated by axisymmetric non-planar entropy waves passing through a flow contraction. Numerically, it has been shown that, at low-frequencies, the sound generated by such entropy waves is independent of the shape of the entropy at the inlet. In the compact limit, the magnitudes of the reflected and transmitted acoustic waves were found to be equal to those obtained for planar entropy waves and, hence, to the predictions of the compact, quasi-one-dimensional and isentropic model of Marble and Candel. At higher frequencies, the non-planar shape effects cause a fall off in the gain of the entropy-to-acoustic transfer functions.

These results have been analysed with a recently developed acoustic analogy theory. The theory was simplified assuming the flow to be inviscid and irrotational and restricting the configurations of interest to low-Mach and low-frequency conditions. The simplified acoustic analogy governing equation were solved using the Green's function method. For the entropy-related sound source term, three models for the profiles of non-plane entropy waves were proposed. It was shown that only when the potential flow streamlines are used as the entropy profiles, the present theoretical model predicts the same sound generation results as Marble and Candel's compact model. The results for non-planar waves were found to be very sensitive to the exact distribution of the entropy perturbations. At slightly higher frequencies when the entropy perturbation cannot be considered compact/uniform across the contraction, the present model predicts the corresponding low-pass filter behaviour for both the acoustic reflection and transmission coefficients.

### Acknowledgements

Aimee Morgans would like to gratefully acknowledge the influence of Shôn Ffowcs Williams (1935-2020) on her career. Shôn supervised her Masters project at Cambridge University in his final year before retirement, encouraging her into a PhD on aeroacoustics. Her Masters project was on flow control (keeping water in the ceiling!), yet his wide-ranging contributions to aeroacoustics soon became apparent, from the Ffowcs Williams - Hawkings equation for her PhD on helicopter noise, to his work on thermoacoustics and entropy noise which inspired her current area of research. His enthusiasm, sense of humour and support of her early career had a long-lasting impact. Dong Yang was supported by the Starting Grant from Southern University of Science and Technology, and Juan Guzmán-Iñigo and Aimee S. Morgans were supported by the European Research Council (ERC) Consolidator Grant AFIRMATIVE (2018–2023, Grant Number 772080) which are acknowledged by the authors.

### Declaration of Conflicting Interests

The author(s) declared no potential conflicts of interest with respect to the research, authorship, and/or publication of this article.

### Funding

The author(s) received no financial support for the research, authorship, and/or publication of this article.

### ORCID iDs

Dong Yang https://orcid.org/0000-0002-0478-1022
Juan Guzmán-Iñigo https://orcid.org/0000-0002-1833-6034

## References


1. Thomas A and Williams GT. Flame noise: sound emission from spark-ignited bubbles of combustible gas. *Proc Roy Soc London Ser A Math Phys Sci* 1966; 294(1439): 449–466. DOI: 10.1098/rspa.1966.0218.
2. Marble FE and Candel SM. Acoustic disturbance from gas non-uniformities convected through a nozzle. *J Sound Vib* 1977; 55: 225–243. DOI: 10.1016/0022-460X(77)90596-X.
3. Bake F, Richter C, Mühlbauer B, et al. The entropy wave generator (EWG): a reference case on entropy noise. *J Sound Vib* 2009; 326(3–5): 574–598. DOI: 10.1016/j.jsv.2009.05.018.
4. Morgans AS and Duran I. Entropy noise: A review of theory, progress and challenges. *Int J Spray Combustion* 2016; 8(4): 285–298. DOI: 10.1177/1756827716651791.
5. Dowling AP and Mahmoudi Y. Combustion noise. *Proc Comb Inst* 2015; 35: 65–100. DOI: 10.1016/j.proci.2014.08.016.
6. Ihme M. Combustion and engine-core noise. *Annu Rev Fluid Mech* 2017; 49: 277–310. DOI: 10.1146/annurev-fluid-122414-034542.
7. Tam CKW, Bake F, Hultgren LS, et al. Combustion noise: modeling and prediction. *CEAS Aeronaut J* 2019; 10(1): 101–122. DOI: 10.1007/s13272-019-00377-2.
8. Goh CS and Morgans AS. The influence of entropy waves on the thermoacoustic stability of a model combustor. *Combustion Sci Technology* 2013; 185: 249–268. DOI: 10.1080/00102202.2012.715828.
9. Stow SR, Dowling AP and Hynes TP. Reflection of circumferential modes in a choked nozzle. *J Fluid Mech* 2002; 467: 215–239. DOI: 10.1017/S0022112002001428.
10. Moase WH, Brear MJ and Manzie C. The forced response of choked nozzles and supersonic diffusers. *J Fluid Mech* 2007; 585: 281–304. DOI: 10.1017/S0022112007006647.
11. Goh CS and Morgans AS. Phase prediction of the response of choked nozzles to entropy and acoustic disturbances. *J Sound Vib* 2011; 330: 5184–5198. DOI: 10.1016/j.jsv.2011.05.016.
12. Giauque A, Huet M and Clero F. Analytical analysis of indirect combustion noise in subcritical nozzles. *J Eng Gas Turbines Power* 2012; 134(11): 111202. DOI: 10.1115/1.4007318.
13. Duran I and Moreau S. Solution of the quasi-one-dimensional linearized Euler equations using flow invariants and the Magnus expansion. *J Fluid Mech* 2013; 723: 190–231. DOI: 10.1017/jfm.2013.118.
14. Magri L, O'Brien J and Ihme M. Compositional inhomogeneities as a source of indirect combustion noise. *J Fluid Mech* 2016; 799: R4. DOI: 10.1017/jfm.2016.397.
15. Magri L. On indirect noise in multicomponent nozzle flows. *J Fluid Mech* 2017; 828: R2. DOI: 10.1017/jfm.2017.591.
16. Yeddula SR, Guzmán-Iñigo J and Morgans AS. A solution for the quasi-one-dimensional linearised Euler equations with heat transfer. *J Fluid Mech* 2022; 936: R3. DOI: 10.1017/jfm.2022.101.
17. Semlitsch B, Hynes T, Langella I, et al. Entropy and vorticity wave generation in realistic gas turbine combustors. *J Propulsion Power* 2019; 35(4): 839–849.
18. Hosseinalipour SM, Fattahi A, Khalili H, et al. Experimental investigation of entropy waves' evolution for understanding of indirect combustion noise in gas turbine combustors. *Energy* 2020; 195: 116978.
19. Greifenstein M, Heinze J, Willert C, et al. Time-resolved temperature profile measurements in the exhaust of a single sector gas turbine combustor at realistic operating conditions. *Experiments in Fluids* 2020; 61(8): 1–12.
20. Weilenmann M and Noiray N. Experiments on sound reflection and production by choked nozzle flows subject to acoustic and entropy waves. *J Sound Vib* 2021; 492: 115799. DOI: 10.1016/j.jsv.2020.115799.
21. Emmanuelli A, Zheng J, Huet M, et al. Description and application of a 2D-axisymmetric model for entropy noise in nozzle flows. *J Sound Vib* 2020; 472: 115163. DOI: 10.1016/j.jsv.2019.115163.
22. Huet M, Emmanuelli A and Le Garrec T. Entropy noise modelling in 2D choked nozzle flows. *J Sound Vib* 2020; 488: 115637. DOI: 10.1016/j.jsv.2020.115637.

23. Goldstein ME. Unsteady vortical and entropic distortions of potential flows round arbitrary obstacles. *J Fluid Mech* 1978; 89: 433–468. DOI: 10.1017/S0022112078002682.
24. Guzmán-Iñigo J, Duran I and Morgans AS. A model for the sound generated by entropy disturbances interacting with isolated blades. In: 2018 AIAA/CEAS Aeroacoustics Conference, Atlanta, GA, 2018, p. 2958. DOI: 10.2514/6.2018-2958.
25. Guzmán-Iñigo J, Duran I and Morgans AS. Scattering of entropy waves into sound by isolated aerofoils. *J Fluid Mech* 2021; 923: A10. DOI: 10.1017/jfm.2021.569.
26. Guzmán-Iñigo J, Baddoo PJ, Ayton LJ, et al. Noise generated by entropic and compositional inhomogeneities interacting with a cascade of airfoils. In: 25th AIAA/CEAS Aeroacoustics Conference, Delft, The Netherlands, 2019, p. 2526. DOI: 10.2514/6.2019-2526.
27. Lighthill MJ. On sound generated aerodynamically i. general theory. *Proceedings Royal Society London Series A Math Phys Sci* 1952; 211(1107): 564–587.
28. Ffowcs Williams JE. Hydrodynamic noise. *Annual Review Fluid Mechanics* 1969; 1(1): 197–222.
29. Morfey CL. Amplification of aerodynamic noise by convected flow inhomogeneities. *J Sound Vibration* 1973; 31(4): 391–397.
30. Ffowcs Williams JE and Howe MS. The generation of sound by density inhomogeneities in low mach number nozzle flows. *J Fluid Mechanics* 1975; 70(3): 605–622.
31. Yang D, Guzmán-Iñigo J and Morgans AS. Sound generation by entropy perturbations passing through a sudden flow expansion. *J Fluid Mech* 2020; 905: R2. DOI: 10.1017/jfm.2020.849.
32. Rolland EO, De Domenico F and Hochgreb S. Theory and application of reverberated direct and indirect noise. *J Fluid Mech* 2017; 819: 435–464. DOI: 10.1017/jfm.2017.183.
33. Howe MS. Indirect combustion noise. *J Fluid Mech* 2010; 659: 267–288. DOI: 10.1017/S0022112010002466.
34. Yang D and Morgans AS. A semi-analytical model for the acoustic impedance of finite length circular holes with mean flow. *J Sound Vibration* 2016; 384: 294–311. DOI: 10.1016/j.jsv.2016.08.006.
35. Donea J and Huerta A. *Finite element methods for flow problems*. Hoboken, NJ: John Wiley & Sons, 2003. DOI: 10.1002/0470013826.
36. Alnæs MS, Blechta J, Hake J, et al. The FEniCS Project Version 1.5. *Archive Numer Software* 2015; 3(100). DOI: 10.11588/ans.2015.100.20553.
37. Logg A, Mardal KA, Wells GN, et al. *Automated Solution of Differential Equations by the Finite Element Method*. Berlin, Germany: Springer, 2012. DOI: 10.1007/978-3-642-23099-8.
38. Crivellini A, D'Alessandro V and Bassi F. A Spalart–Allmaras turbulence model implementation in a discontinuous Galerkin solver for incompressible flows. *J Computational Physics* 2013; 241: 388–415. DOI: 10.1007/s10494-015-9656-7.
39. Amestoy PR, Duff IS, Koster J, et al. A fully asynchronous multifrontal solver using distributed dynamic scheduling. *SIAM J on Matrix Analysis Applications* 2001; 23(1): 15–41. DOI: 10.1137/S0895479899358194.
40. Amestoy PR, Guermouche A, L'Excellent JY, et al. Hybrid scheduling for the parallel solution of linear systems. *Parallel Computing* 2006; 32(2): 136–156. DOI: 10.1016/j.parco.2005.07.004.
41. Guzmán-Iñigo J, Yang D, Gaudron R, et al. On the scattering of entropy waves at sudden area expansions. 2021. *Manuscript under review* 2021. ArXiv Preprint arXiv:2111.13043. https://arxiv.org/abs/2111.13043.
42. Seybert AF and Ross DF. Experimental determination of acoustic properties using a two-microphone random-excitation technique. *J Acoust Soc Am* 1977; 61(5): 1362–1370. DOI: 10.1121/1.381403.
43. Poinsot T, Le Chatelier C, Candel SM, et al. Experimental determination of the reflection coefficient of a premixed flame in a duct. *J Sound Vib* 1986; 107(2): 265–278. DOI: 10.1016/0022-460X(86)90237-3.
44. Schleicher RM and Howe MS. On the interaction of sound with an annular aperture in a mean flow duct. *J Sound Vib* 2013; 332(21): 5594–5605. DOI: 10.1016/j.jsv.2013.05.006.